Chemical Engineering Journal 442 (2022) 136157

Contents lists available at ScienceDirect

Chemical Engineering Journal

journal homepage: www.elsevier.com/locate/cej

Constructing crystalline redox catalyst to achieve efficient CO_2 photoreduction reaction in water vapor

Xiao-Xin Li [a,b,1], Lei Zhang [b,1], Lin Yuan [c,1], Tong Wang [c], Long-Zhang Dong [c], Kai Huang [a,*], Jiang Liu [b,c,*], Ya-Qian Lan [b]

[a] School of Chemistry and Chemical Engineering, Southeast University, No.2, Southeast University Road, Nanjing 211189, PR China
[b] School of Chemistry, South China Normal University, No.55, West of Zhongshan Avenue, Guangzhou 510631, PR China
[c] Jiangsu Collaborative Innovation Centre of Biomedical Functional Materials, Jiangsu Key Laboratory of New Power Batteries, School of Chemistry and Materials Science, Nanjing Normal University, No. 1, Wenyuan Road, Nanjing 210023, PR China

ARTICLE INFO

Keywords:
Reduction-oxidation cluster-based compounds
Copper (I) photocatalyst
Polyoxometalate
Artificial photosynthesis
Photocatalytic reaction

ABSTRACT

Artificial photosynthesis, coupling CO_2 photoreduction and water photooxidation reactions, is an important and green means to convert CO_2. Compared with traditional multiphasic heterojunctions, monophasic photocatalysts for artificial photosynthesis are still very rare. Here we construct a crystalline overall reaction catalyst, **RO-4**, by connecting reductive $\{Cu^{I}_{8}\}$ and oxidative $\{PMo_8V_6O_{42}\}$ clusters with bridging oxygen atoms, which allow the photogenerated electrons to transfer easily between the redox clusters. Under light irradiation, **RO-4** can achieve efficient artificial photosynthesis with a high CO production activity of 20.06 μmol $g^{-1}h^{-1}$ (>99.5% selectivity) along with O_2 release. Furthermore, in situ DRIFTS and DFT calculations uncover the related reaction intermediates and CO_2 photoreduction mechanism. This work validates a feasible strategy to engineer monophasic crystalline RO photocatalysts for efficient artificial photosynthetic overall reaction.

1. Introduction

The increasingly depleted non-renewable energy sources and the severe greenhouse effect have reached the critical line of sustainable development [1–3]. Reducing CO_2 to fuels (CO, CH_4, etc) has been regarded as one of the most efficient ways to mitigate the greenhouse effect and close the carbon cycle [4–8]. So far, CO_2 reduction has often been achieved by hydrogenation reaction under high temperature and pressure conditions or the presence of noble metals like Ru, Pt catalysts [9,10]. In contrast, artificial photosynthesis involving photocatalytic CO_2 reduction reaction (CO_2RR) and water oxidation reaction (WOR) is a low-cost and environment-friendly strategy to reuse CO_2 [11–13]. However, the half reaction of WOR is tough to achieve dynamically, most catalytic systems currently need to add additional organic sacrificial agents to receive electrons in the reactions, which would cause environmental pollution and increase the difficulty of segregating the liquid product. Thus, it is a goal to design and synthesize photocatalysts that contain active sites for both CO_2RR and WOR to achieve the artificial photosynthetic overall reaction.

Polyoxometalate metal–organic framework (POMOF) is a kind of crystalline material with precise structure information, which couples the advantages of both MOF[14,15] and Polyoxometalate (POM) [16–20] (e.g. excellent redox capability and high structural tunability) [21]. Furthermore, the well-defined structures can help to identify the active sites and understand the structure–activity relationship [22]. Based on these strengths, POMOFs have been widely utilized as photocatalysts applied to CO_2 reduction or water splitting, and further explore the reaction mechanism. Importantly, the oxidative POM units can be easily connected to reductive transition metal clusters. The coexistence of reductive and oxidative components to construct reduction–oxidation (RO) catalysts enable effectively coupling CO_2RR and WOR simultaneously [23–25]. Recently, Cu(I)-based catalysts have attracted much attention for their outstanding performance in catalytic hydrogen evolution reaction (HER) and CO_2RR due to their good reducibility, which can be the candidate as the reductive site in RO photocatalyst [26–31]. On the other hand, phosphovanadomolybdate (**PMoV**) often exhibits excellent oxidability applied to various oxidation reactions [32]. Hence, it may promote the efficiency of artificial photosynthesis by assembling

* Corresponding authors at: School of Chemistry, South China Normal University, No.55, West of Zhongshan Avenue, Guangzhou 510631, PR China.
E-mail addresses: huangk@seu.edu.cn (K. Huang), liuj@njnu.edu.cn (J. Liu).
[1] These authors contributed equally to this work.

https://doi.org/10.1016/j.cej.2022.136157
Received 12 January 2022; Received in revised form 19 March 2022; Accepted 31 March 2022
Available online 1 April 2022

a specific Cu(I) cluster and **PMoV** into a POMOF.

Based on the above consideration, a novel reduction–oxidation POMOF, **RO-4** ($Cu_8Cl[PMo_8V_6O_{42}](p\text{-}tr_2Ph)_4{\cdot}8H_2O$), was synthesized by in situ hydrothermal method (see Supporting Information for detailed methods). In **RO-4**, the eight nuclear copper cluster {Cu_8} and {$PMo_8V_6O_{42}$} can be catalytic sites for accomplishing CO_2RR and WOR. The calculated band structure of **RO-4** obtained from ultraviolet and visible spectrophotometry (UV–vis), Mott-Schottky plots and ultraviolet photoelectron spectrometer (UPS) indicate that **RO-4** can realize artificial photosynthetic overall reaction. Under the light irradiation, **RO-4** showed excellent photocatalytic activity, of which the yield of CO_2-to-CO conversion was up to 20.06 μmol $g^{-1}h^{-1}$ along with O_2 release. The DFT calculation results showed that the CO_2RR and WOR probably occur on {Cu_8} cluster and {$PMo_8V_6O_{42}$}, respectively. In comparison, another photocatalyst **CuL** that consisted of p-tr_2Ph and Cu ions but without {$PMo_8V_6O_{42}$} only showed a weak photocatalytic performance

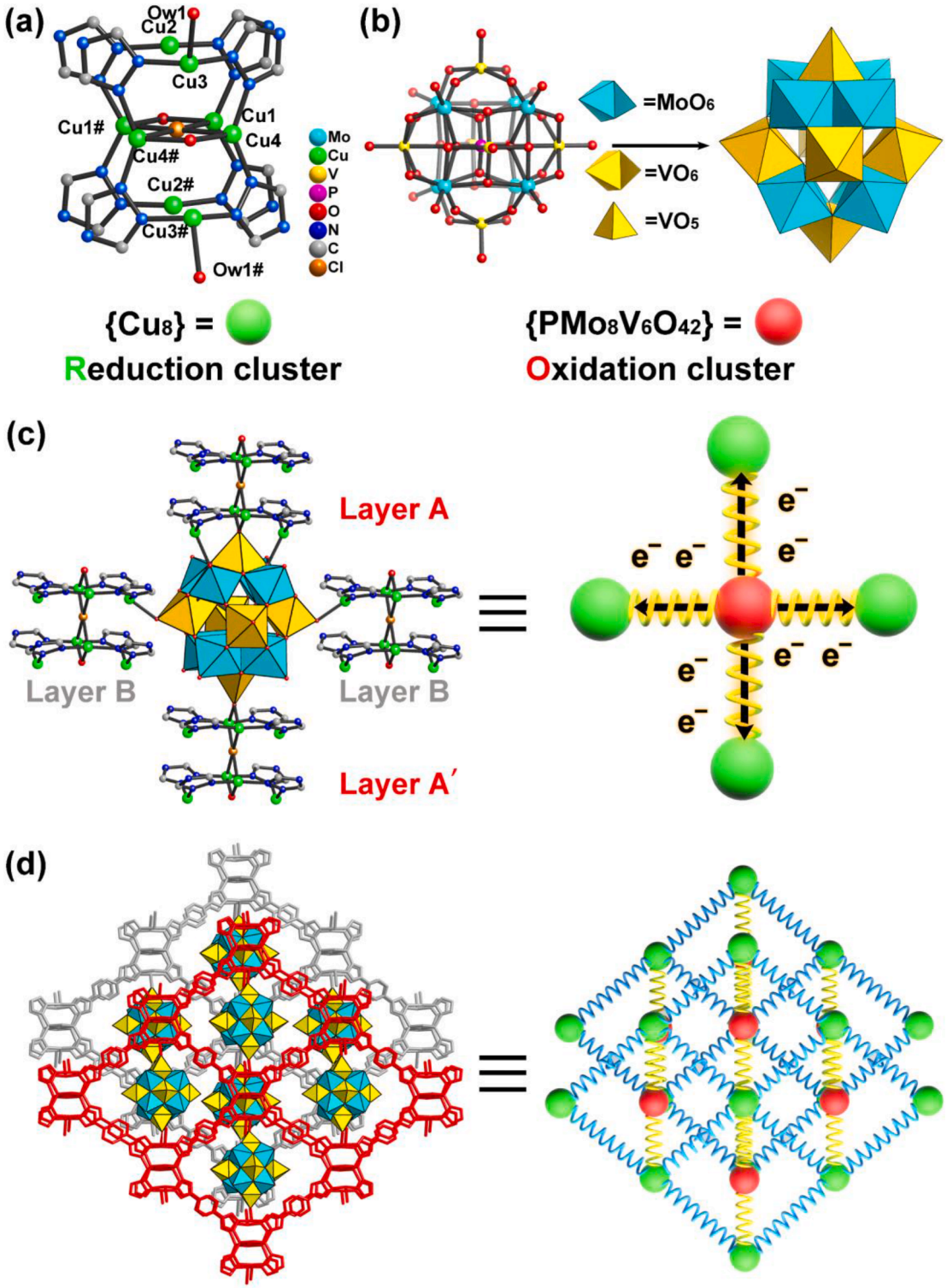

Fig. 1. Summary of the structure of RO-4. (a) The structure of {Cu_8} cluster; (b) The coordination environment of {$PMo_8V_6O_{42}$} node; (c) Top view of 2D layers in AB-stacking mode constructed from {Cu_8} and ligands; (d) Structure of the 3D framework. Mo, blue; Cu, green; V, yellow; P, pink; C, gray; N, blue; O, red; Cl, brown.

compared to **RO-4**, indicating that the coexistence of reductive {Cu_8} cluster and oxidative {$PMo_8V_6O_{42}$} cluster is the key factor to achieve the overall reaction efficiently.

2. Results and discussions

2.1. Synthesis and characterizations of RO-4 photocatalysts

Single-crystal X-ray diffraction (SCXRD) indicated that **RO-4** crystallizes in the orthorhombic system with a *Cmcm* space group, and the asymmetric unit contains 1/2 {$PMo_8V_6O_{42}$} cluster, four Cu ions, one *p*-tr_2Ph, one μ_4-Cl ion, one coordinated and two free water molecules (Fig. S2). As shown in Fig. 1a, eight Cu ions, eight triazoles from ligands, two μ_2-O atoms and one μ_4-Cl ion form an octanuclear {Cu_8} cluster together. There are three crystallographic independent Cu atoms in {Cu_8}. Four Cu ions (Cu1, Cu1#, Cu4, Cu4#) are 4-coordinated tetrahedral configuration with two N atoms from ligands, one μ_2-O atom and one μ_4-Cl ion. Two Cu ions (Cu2, Cu2#) are triangular pyramidal configuration coordinated with two N atoms and one terminal O atom from {$PMo_8V_6O_{42}$}. The rest two Cu ions (Cu3, Cu3#) are tetrahedral configuration coordinated with two N atoms, one O atom from {$PMo_8V_6O_{42}$} and one water molecule. Each {Cu_8} cluster links eight ligands to form a 2D layer, which packs in AB-stacking mode (Fig. S3). {$PMo_8V_6O_{42}$} cluster is a heteroatom α-Keggin structure in which four {Mo_2VO_{13}} units are corner-linked to the central {PO_4} and two {VO_5} units caps are on either side of the structure (Fig. 1b and S4)[33–35]. In order to understand the connection mode of oxidative and reductive clusters, the coordination environments of {Cu_8} and {$PMo_8V_6O_{42}$} are analyzed. In Fig. S5, each {Cu_8} cluster connected four {$PMo_8V_6O_{42}$} clusters in three different coordination modes. The top of POM node connects to {Cu_8} cluster with four Cu–O bonds. On the mid of the kegging node, two opposite terminal O atoms connect with two {Cu_8} clusters by Cu–O bonds. The bottom of POM node links with a {Cu_8} cluster by two Cu–O bonds. In the cavity of layers, {$PMo_8V_6O_{42}$} were filled and connected with four {Cu_8} clusters in three adjacent layers (Fig. 1c). Due to the presence of POMs, the 2D layers are assembled into a 3D framework (Fig. 1d). In addition, the {Cu_8} cluster can be regarded as an 8-connected node for concatenating four other {Cu_8} clusters and four {$PMo_8V_6O_{42}$} clusters, in which the {$PMo_8V_6O_{42}$} can be regarded as a four-connected node. In this regard, **RO-4** reveals a topology with the Schläfli symbol of {4^{12}. 6^{16}} {4^5. 6}, which shows a new type of topology (Fig. S6). In order to explore the importance of the coexistence of oxidation and reduction sites, **CuL** composed of Cu(I) ions and *p*-tr_2Ph ligand was further synthesized. **CuL** crystallizes in the monoclinic system with a $P2_1/n$ space group. An asymmetric unit contains two Cu ions, one *p*-tr_2Ph, two Cl ions, one free water molecule (Fig. S7). The ligands link with {Cu_2Cl_2} cluster to extend into a 1D chain (Fig. S8 and S9).

The powder X-ray diffraction (PXRD) pattern of the obtained **RO-4** was well-matched with the curve simulated from single-crystal X-ray diffraction, proving the high purity of the samples (Fig. S10). To evaluate the chemical stability of **RO-4**, fresh crystals are soaked in different aqueous solutions for a period of 24 h. The unchanged peaks disclose that **RO-4** can remain structural integrity in 0.1 M HCl and 0.1 M NaOH solutions (Fig. S11). The thermal stability of **RO-4** was tested through thermogravimetric analysis (TGA). There is no significant weight loss before 300 °C, meaning that **RO-4** has good thermodynamic stability (Fig. S12). The valence states of metal ions in **RO-4** were analyzed by X-ray photoelectron spectroscopy (XPS). As shown in Fig. S13, all the elements in **RO-4** can be observed from the full-scan spectrum. The V 2p peak located at 517.02 eV reveals that the valence state V ions is + 4 in **RO-4**. The Mo 3d peak can be ascribed to Mo^{5+} and Mo^{6+}, which is consistent with the previous report. The Cu 2p spectrum shows two main peaks at 932.2 and 952.1 eV corresponding to $Cu^{+/0}$ and Cu^{2+}, of which the weak Cu^{2+} peak may generate from the part of surface Cu ions oxidized in air. Most of the Cu ions are still Cu^{I} in the **RO-4**, which can also be evidenced in the Auger Cu LMM (LM2) spectrum.

The light absorption of **RO-4**, **CuL** and {$PMo_8V_6O_{42}$} were examined through UV–vis diffuse reflectance spectroscopy, of which the purity of {$PMo_8V_6O_{42}$ } and **CuL** were also proved by the well-matched PXRD patterns (Fig. S14 and S15). In Fig. 2a, **RO-4** and {$PMo_8V_6O_{42}$} have similar spectral absorption regions about 300 ~ 1100 nm, while **CuL** only has ultraviolet absorption for the lack of phosphovanadomolybdate, indicating that the POM in **RO-4** is response for light absorption. This result also agrees with their corresponding crystal color under the optical microscope (Fig. S17). The band gaps (Eg) of **RO-4**, **CuL** and {$PMo_8V_6O_{42}$} were further evaluated from original UV–Vis-NIR data with Kubelka-Munk formula: $(\alpha h\nu = C(h\nu - E_g)^{1/2})$, which were calculated to be 1.75, 2.95, 1.66 eV respectively, indicating that all of them have the characteristics of the semiconductor (Fig. 2b). The position of the lowest unoccupied molecular orbital (LUMO) of **RO-4** and {$PMo_8V_6O_{42}$} were determined by ultraviolet photoelectron spectroscopy (UPS). By subtracting the width of the He I UPS spectrum from the excitation energy (eV), the final calculation results are 1.15, 1.86 and 1.03 eV (vs NHE, pH = 7) of **RO-4**, **CuL** and {$PMo_8V_6O_{42}$}, respectively (Fig. 2c, S18 and S19) [36]. On the other hand, Mott-Schottky plot measurements were performed to further verify the accuracy of the semiconductor band structures on **RO-4**, **CuL** and {$PMo_8V_6O_{42}$} at frequencies of 1000, 1500, and 2000 Hz (Fig. 2d, S20 and S21). The obtained C^{-2} curves with *x*-axis were intersected at −0.85 (**RO-4**), −1.20 (**CuL**), −0.82 V ({$PMo_8V_6O_{42}$}) vs Ag / AgCl. The highest occupied molecular orbital (HOMO) positions were calculated to be −0.65, −1.00, −0.62 V vs NHE, respectively, which are consistent with the consequence of UPS. Fig. 2e shows the band structures of **RO-4**, **CuL** and {$PMo_8V_6O_{42}$}. LUMO and HOMO values are converted to normal hydrogen electrodes (NHE, pH = 7) in volts (right *y*-axis). It can be found that all the LUMO positions of **RO-4**, **CuL** and {$PMo_8V_6O_{42}$} are suitable for reducing CO_2 to most products like CO, CH_4, etc[37,38]. The values of their HOMO are all more positive than the oxidation potential of O_2/H_2O, which indicates that all of them can theoretically be invoked as photocatalysts for the entire redox reaction. The ability of the surface of the **RO-4** to absorb CO_2 molecules also makes it feasible to be utilized as photocatalyst for CO_2RR (Fig. S22). In addition, photocurrent profiles of **RO-4**, **CuL** and {$PMo_8V_6O_{42}$} show they have sharp and sensitive transient photocurrent response when the light is periodically switched under irradiation (Fig. 2f, S23 and S24). The near two times higher response of **RO-4** than **CuL** and {$PMo_8V_6O_{42}$} reflects the best separating efficiency of photoinduced electron and hole pairs of **RO-4**. The smaller resistance of **RO-4** suggested that the photogenerated charges are more conducive to migrate to the surface of the catalyst for photocatalytic reactions (Fig. S25). Importantly, time-resolved fluorescence decay spectra (Fig. S26 and Table S4) were carried out to evaluate the specific charge carrier dynamics [39]. The longer average lifetime of **RO-4** (2.88 ns) than {$PMo_8V_6O_{42}$} (2.48 ns) revealed that the photogenerated charges can survive longer to occur photocatalytic reactions (CO_2RR and WOR) when {$PMo_8V_6O_{42}$} links with {Cu_8} into **RO-4**.

2.2. Photocatalytic performance of CO_2RR and WOR

Due to the well-matched band structure and concomitant oxidation/reduction sites, the photocatalytic overall reactions were investigated in the gas–solid system[40,41] under light irradiation (λ = 300 ~ 1100 nm) without additional co-catalyst, photosensitizer, or sacrificial agent. All the experimental details were described in the Supporting Information. As expected, **RO-4** showed excellent performance of CO_2-to-CO photoreduction with H_2O-to-O_2 photooxidation. After 4 h of light irradiation, **RO-4** exhibited a high CO yield (80.24 μmol g^{-1}) and selectivity (>99.5 %) along with O_2 production (Fig. S27). Through detecting CO yield per hour, a roughly linear relationship between reaction time and target product was obtained (Fig. 3a). No gas products observed in the argon atmosphere indicate the CO is converted from CO_2 rather than the decomposition of catalyst. Importantly, to explore the importance of the coexistence of Cu cluster and POM, the photocatalytic performance of

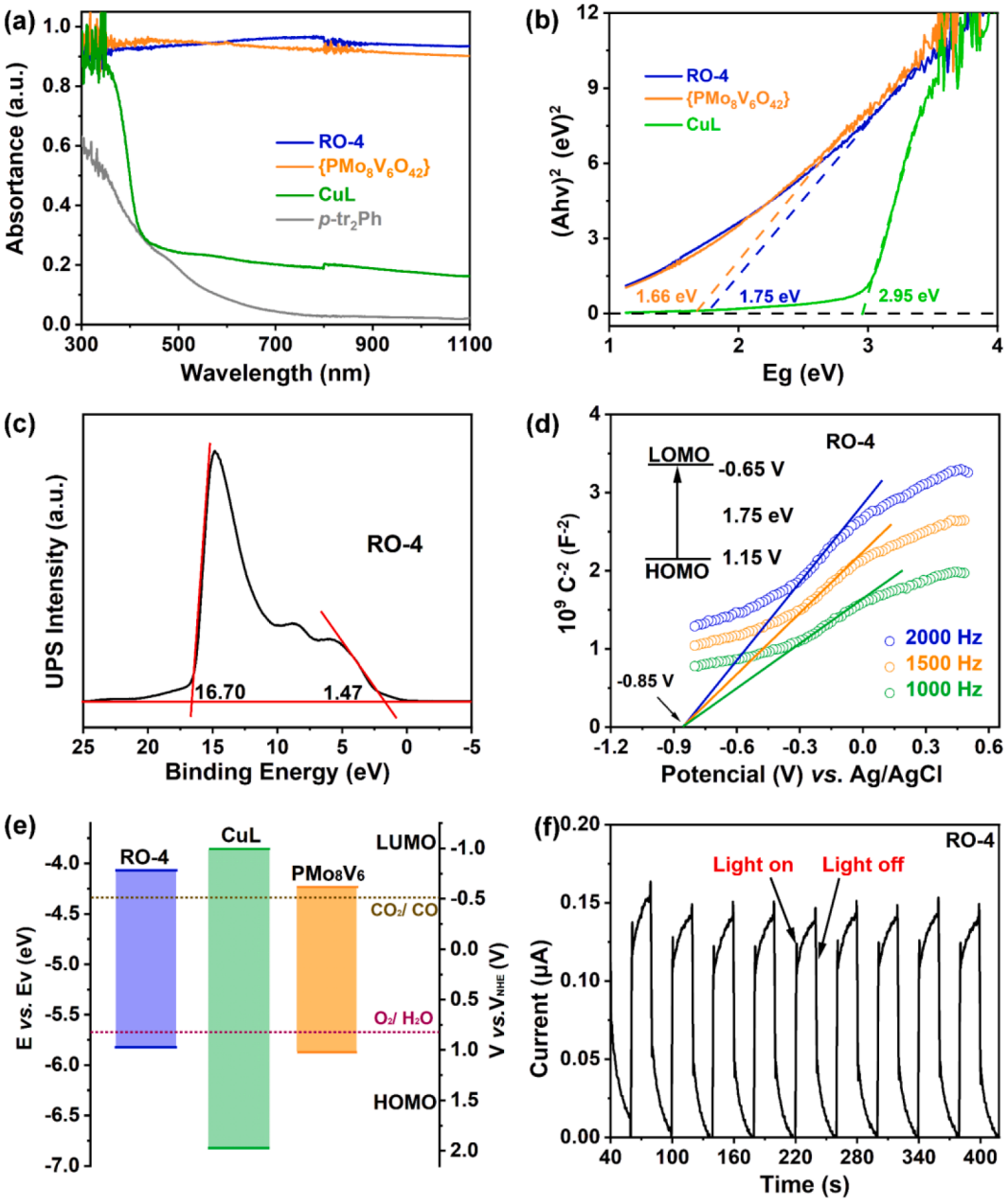

Fig. 2. Optical characterizations of photocatalysts. (a) Solid-state UV–Vis absorption spectra of **RO-4**, $\{PMo_8V_6O_{42}\}$, **CuL** and p-tr$_2$Ph. (b) Tauc plots of **RO-4**, $\{PMo_8V_6O_{42}\}$, **CuL**. (c) UPS, (d) Mott-Schottky plots of **RO-4**. (e) The energy band structures diagram for **RO-4**, $\{PMo_8V_6O_{42}\}$, **CuL**. (f) Transient photocurrent curve of **RO-4** that measured in 0.5 M Na_2SO_4 aqueous solution.

CuL with Cu^I active center (Fig. S28) and $\{PMo_8V_6O_{42}\}$ were evaluated under the same condition. Within 4 h, the CO yield catalyzed by **RO-4** was much higher than 22.0 μmol g^{-1} of bulk $\{PMo_8V_6O_{42}\}$ cluster and 26.0 μmol g^{-1} of **CuL** (Fig. 3b and Table S5). Furthermore, the physical mixture of $\{PMo_8V_6O_{42}\}$ and **CuL** according to the molecular weight in **RO-4** was also tested (entry 4). The yield of CO is obviously lower than **RO-4**, indicating the necessity of direct bonding of the two components. Besides CO, the production of CH_4 (less than 0.1 μmol g^{-1}) was below the minimum standard of the detection line. Additionally, no secondary H_2 was detected during the overall reaction (Fig. S29), which demonstrates the high selectivity of **RO-4**. In order to eliminate the influence of air on the quantification of O_2 products, the photocatalytic tests in an online system were performed along with **RO-4** as the catalyst. The mole ratio of produced CO to O_2 is close to 2/1, which corresponds to the ratio of transferred electrons of catalytic process, indicating the occurrence of the artificial photocatalytic overall reaction (Fig. S30). The cycle test was carried out to evaluate the durability of the photocatalyst by only refilling the saturated CO_2 and reintroducing fresh water. As shown in Fig. 3c and Table S6, **RO-4** retains *ca.* 92% of its original activity after 15 cycles (total 60 h). The durability of **RO-4** as photocatalyst was also evaluated under continuous irradiation, the production of CO increased almost linearly at least 15 h (Fig. S31). There were no significant changes in the PXRD, FTIR and XPS patterns (Fig. S32-S34), which proved the structural and chemical stability of **RO-4** during the photocatalytic process. In order to study the influence factors of CO_2 photoreduction, a series of comparative experiments were carried out and the results were shown in Table S5. When the system was absence of light (entry 5) or **RO-4** (entry 6), no product could be detected, which indicated that **RO-4** is really the catalyst for the reaction and the conversion process is a light-driven catalytic reaction. When **RO-4** is used as the photocatalyst for the system lacking H_2O (entry 7), only trace of CO could be observed, which maybe utilize coordinated water in the **RO-4**.

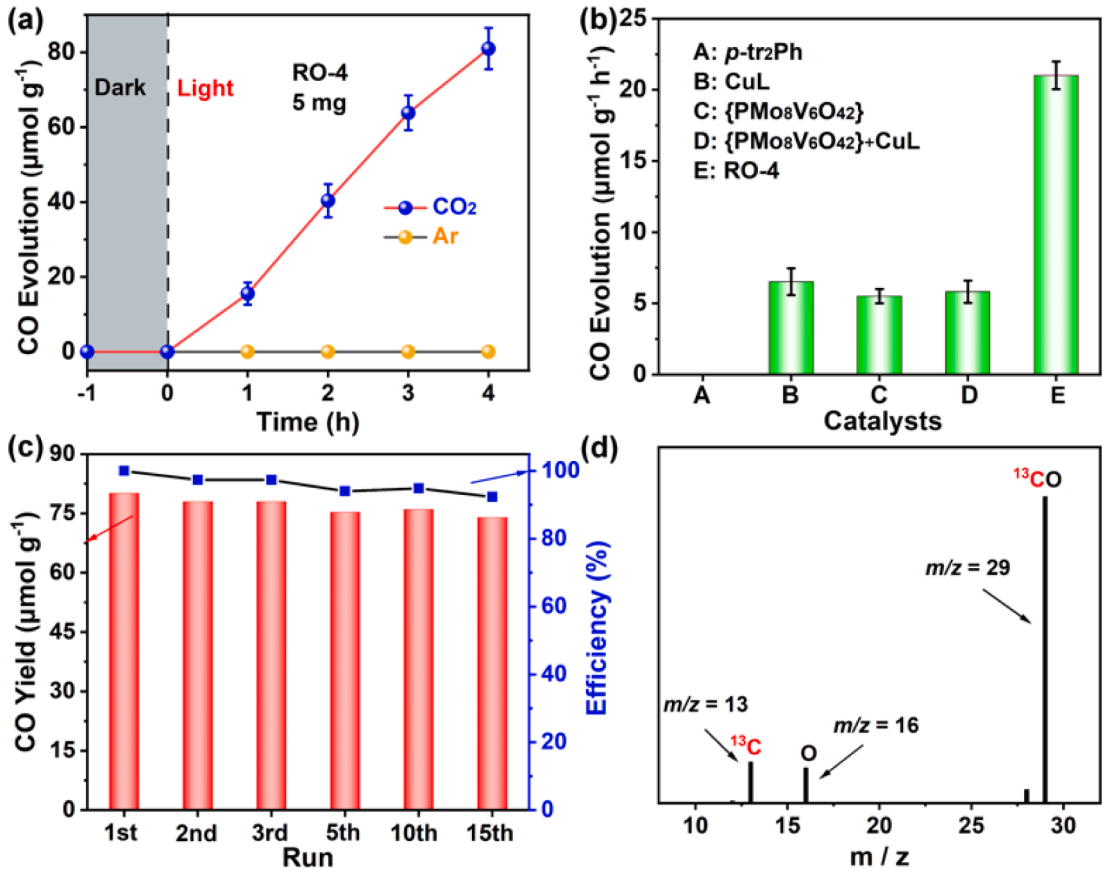

Fig. 3. Photocatalytic CO_2 reduction properties over RO-4. (a) In different atmospheres. (b) The yield of CO in a series of comparative tests on different photocatalysts. (c) Durability measurements of **RO-4** in fifteen continuous runs (4-hour test per cycle). (d) Mass spectrum of produced ^{13}CO (m / z = 29) catalyzed by **RO-4** in the photocatalytic reduction under $^{13}CO_2$.

It suggested that H_2O is the sacrificial agent.

To confirm where the catalytic reaction took place, the pure H_2L (entry 8) was examined, there was not any product that could be detected, suggesting both the CO_2RR and WOR were accomplished by metal sites. ^{13}C and ^{18}O isotope experiments were performed to search for the source of carbon and oxygen in the productions through a gas chromatography-mass spectrometer (GC–MS). After carrying out the same photocatalytic test but using $^{13}CO_2$ as atmosphere, the obvious *m/z* peaks of 13, 16, 29 corresponding to ^{13}C, O, and ^{13}CO can be found, indicating the produced CO was indeed converted from CO_2 (Fig. 3d). The increasing absolute abundance of ^{13}C labled CO over time further proved it (Fig. S35). The distinct *m/z* peak at 36 corresponding to $^{18}O_2$ indicates the occurrence of water oxidation when using $H_2{}^{18}O$ as reactant (Fig. S36).

The migration direction of photogenerated charges was judged by in situ XPS measurements. As shown in Fig. S37, high-resolution Cu LM2 XPS spectrum reveals that the Cu ions in **RO-4** are + 1 oxidation state in the dark and N_2 atmosphere [42]. When **RO-4** was exposed under light irradiation for 30 min, a peak at 918.6 eV corresponding to Cu^0 appeared, indicating that the Cu ions receive photoelectrons and are reduced. On this basis, when the atmosphere was further changed to CO_2, the Cu^0 XPS signal was obviously attenuated. It can be interpreted as part of Cu^0 centers give electrons to CO_2 molecules and catalyze CO_2RR, and then turn back to + 1 oxidation state at the same time. These results not only demonstrated that photogenerated electrons can migrate from POM to $\{Cu_8\}$ clusters under light irradiation, but also indicate that $\{Cu_8\}$ clusters act as photocatalytic sites for CO_2RR. To evaluate the underlying process for the CO_2 photoreduction with **RO-4** as a photocatalyst, in situ diffuse reflectance infrared Fourier transform spectroscopy (DRIFTS) was investigated in a mixed atmosphere of CO_2 and water vapor (Fig. 4a). After 30 min of light irradiation, the spectrum exhibits five characteristic peaks of 1319, 1506, 1540, 1636 and 1652 cm^{-1} which can be confirmed to the co-adsorption of CO_2 and H_2O on the **RO-4** surface. Meanwhile, the peaks located at 1414, 1436 and 1454 cm^{-1} confirms to HCO_3^- group, and the absorption peaks occurred in 1557, 1521, 1243 and 1714 cm^{-1} assigns to COO^- species, respectively. Notably, the peaks around 1396 and 1250 cm^{-1} belong to the COOH* group, which is treated as an intermediator during CO_2 reduction to CO. Moreover, the significant peak absorbance of CO* (2060 cm^{-1}) supports the formation of CO during the photocatalytic CO_2 reduction [43–51].

2.3. DFT calculations and exploration on reaction mechanism

Based on the intermediates detected by in situ DRIFTS, we further calculate the energy changes of the process of photocatalytic CO_2 reduction by density functional theory (DFT). The calculation results reveal that the whole process of CO_2-to-CO conversion goes through four steps: CO_2 activation, hydrogenation, dehydration and CO desorption (Fig. 4b), in which CO desorption is considered the potential-determining step (PDS). The computed values Gibbs free energy changes are all less than 0.4 eV at every step, indicating that **RO-4** is a prospective photocatalyst for CO_2RR (Fig. 4c). Through the theoretical results, a feasible mechanism can be suggested explaining artificial photosynthesis. Firstly, the photoelectron-hole pairs are excited in $\{PMo_8V_6O_{42}\}$ of **RO-4** upon light irradiation and then the photoelectrons transfer to the $\{Cu_8\}$ cluster. The $\{Cu_8\}$ receives photoelectrons to the adsorbed CO_2 for CO evolution, simultaneously the photogenerated holes in $\{PMo_8V_6O_{42}\}$ group achieve the H_2O oxidation. Under this catalysis system consisting of light, CO_2 and water vapor, **RO-4** as a photocatalyst makes the artificial photosynthetic overall reaction

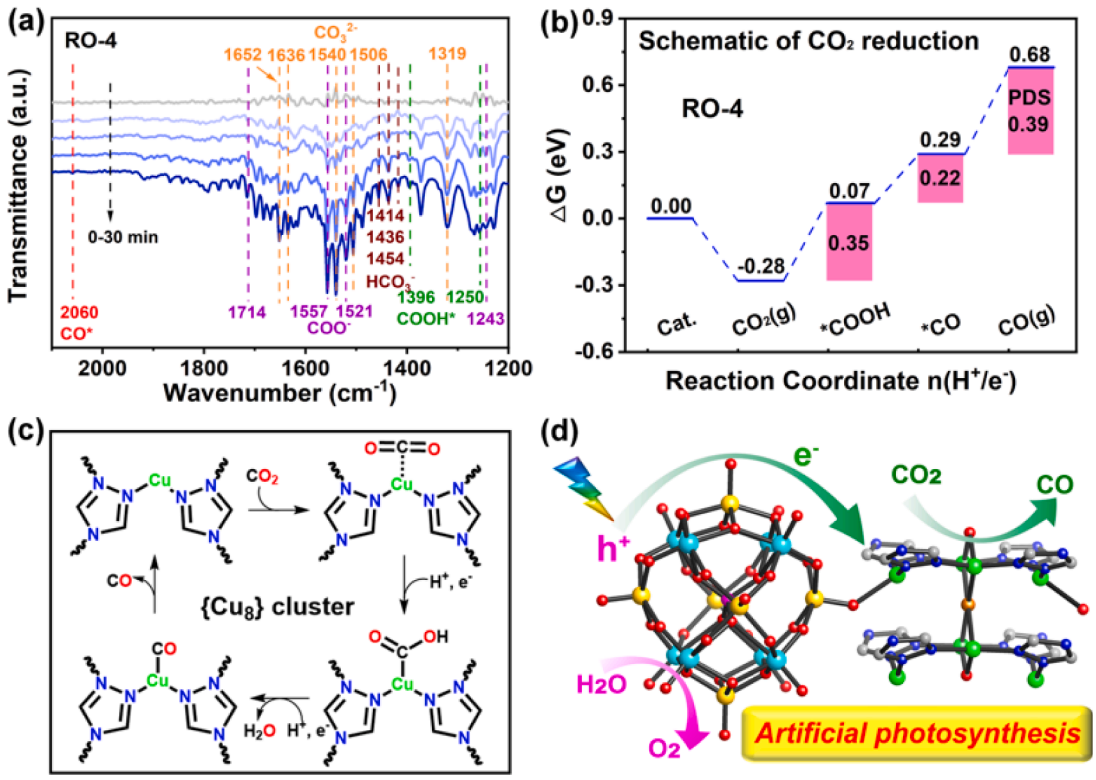

Fig. 4. Proposed mechanism of CO_2RR and WOR catalyzed by RO-4. a) In situ DRIFTS spectrum for **RO-4** under irradiation. b) Gibbs free energy diagram of **RO-4** for photocatalytic CO_2 reduction based on DFT calculation. c) Reaction pathway for the photocatalytic CO_2 reduction on {Cu_8}. d) Scheme of the feasible mechanism for artificial photosynthesis alone with **RO-4** as catalyst.

accomplished steadily (Fig. 4d).

3. Conclusion

In summary, we have designed and synthesized a crystalline photocatalyst, **RO-4**, which was assembled with reductive {Cu_8} clusters and oxidative {$PMo_8V_6O_{42}$} clusters through bridging O atoms, to achieve artificial photosynthesis effectively. The CO_2RR and WOR are respectively occurred on {Cu_8} and {$PMo_8V_6O_{42}$} motifs, and the bridging O atoms showed the advantage of transferring photogenerated electrons rapidly. Thus, photogenerated charges can be efficiently separated between reductive and oxidative sites, resulting in that **RO-4** reveals a much higher CO yield (20.06 μmol $g^{-1}h^{-1}$, > 99.5 % selectivity) than that of **CuL** (6.50 μmol $g^{-1}h^{-1}$) and {$PMo_8V_6O_{42}$} (5.50 μmol $g^{-1}h^{-1}$). These results verify the rationality of our design idea in constructing RO-based photocatalyst. More importantly, the ^{13}C and ^{18}O isotopic labeling experiments are carried out to prove that the produced CO and O_2 are indeed derived from CO_2 and H_2O. In addition, the intermediates of the reaction process were successfully captured by in-situ DRIFT. Based on the obtained intermediates and precise single crystal structure of **RO-4**, it allows us to in-depth understand the photocatalytic reaction mechanism by DFT calculation. This work rarely utilizes monophasic coordination compound to achieve artificial photosynthetic whole reaction. It not only broadens the application of crystalline coordination compounds in the field of CO_2 photoreduction reaction in water vapor, but also may provide guidance in designing novel monophasic photocatalyst applied to other overall reactions like water splitting.

Declaration of Competing Interest

The authors declare that they have no known competing financial interests or personal relationships that could have appeared to influence the work reported in this paper.

Acknowledgements

This work was financially supported by NSFC (No. 92061101, 21871141, 21871142, 22071109 and 51778142); the China Civil Aviation Science and Technology Innovation Fund (MHRD20140215); the Excellent Youth Foundation and Distinguished Youth Foundation of Jiangsu Province Natural Science Foundation (NO. BK20211593); the GuangDong Basic and Applied Basic Research Foundation (No. 2021A1515110429); Priority Academic Program Development of Jiangsu Higher Education Institutions and the Foundation of Jiangsu Collaborative Innovation Center of Biomedical Functional Materials.

Appendix A. Supplementary data

Supplementary data to this article can be found online at https://doi.org/10.1016/j.cej.2022.136157.

References

[1] A.W. Schäfer, S. Yeh, A holistic analysis of passenger travel energy and greenhouse gas intensities, Nat. Sustain. 3 (6) (2020) 459–462.
[2] S. Cestellos-Blanco, H. Zhang, J.M. Kim, Y.-X. Shen, P. Yang, Photosynthetic semiconductor biohybrids for solar-driven biocatalysis, Nat. Catal. 3 (3) (2020) 245–255.
[3] S.R. Nicholson, N.A. Rorrer, A.C. Carpenter, G.T. Beckham, Manufacturing energy and greenhouse gas emissions associated with plastics consumption, Joule 5 (3) (2021) 673–686.
[4] J. Fu, K. Jiang, X. Qiu, J. Yu, M. Liu, Product selectivity of photocatalytic CO_2 reduction reactions, Mater. Today 32 (2020) 222–243.
[5] W. Zhang, A.R. Mohamed, W.-J. Ong, Z-Scheme Photocatalytic Systems for Carbon Dioxide Reduction: Where Are We Now? Angew. Chem. Int. Ed. 59 (51) (2020) 22894–22915.
[6] X. Li, J. Yu, M. Jaroniec, X. Chen, Cocatalysts for Selective Photoreduction of CO_2 into Solar Fuels, Chem. Rev. 119 (6) (2019) 3962–4179.
[7] K. Su, G.-X. Dong, W. Zhang, Z.-L. Liu, M. Zhang, T.-B. Lu, In Situ Coating $CsPbBr_3$ Nanocrystals with Graphdiyne to Boost the Activity and Stability of Photocatalytic CO_2 Reduction, ACS Appl Mater Interfaces 12 (2020) 50464–50471.

[8] Y.-F. Mu, C. Zhang, M.-R. Zhang, W. Zhang, M. Zhang, T.-B. Lu, Direct Z-Scheme Heterojunction of Ligand-Free $FAPbBr_3$/α-Fe_2O_3 for Boosting Photocatalysis of CO_2 Reduction Coupled with Water Oxidation, ACS Appl Mater Interfaces 13 (2021) 22314–22322.

[9] P. Zhou, Y. Chao, F. Lv, J. Lai, K. Wang, S. Guo, Designing noble metal single-atom-loaded two-dimension photocatalyst for N_2 and CO_2 reduction via anion vacancy engineering, Sci. Bull. 65 (9) (2020) 720–725.

[10] M. Humayun, H. Ullah, L. Shu, X. Ao, A.A. Tahir, C. Wang, W. Luo, Plasmon Assisted Highly Efficient Visible Light Catalytic CO_2 Reduction Over the Noble Metal Decorated Sr-Incorporated g-C_3N_4, Nanomicro Lett. 13 (2021) 209.

[11] L.-Z. Dong, L. Zhang, J. Liu, Q. Huang, M. Lu, W.-X. Ji, Y.-Q. Lan, Stable Heterometallic Cluster-Based Organic Framework Catalysts for Artificial Photosynthesis, Angew. Chem. Int. Ed. 59 (7) (2020) 2659–2663.

[12] S. Ye, C. Ding, M. Liu, A. Wang, Q. Huang, C. Li, Water Oxidation Catalysts for Artificial Photosynthesis, Adv. Mater. 31 (2019) 1902069.

[13] L.-Y. Wu, Y.-F. Mu, X.-X. Guo, W. Zhang, Z.-M. Zhang, M. Zhang, T.-B. Lu, Encapsulating Perovskite Quantum Dots in Iron-Based Metal-Organic Frameworks (MOFs) for Efficient Photocatalytic CO_2 Reduction, Angew. Chem. Int. Ed. 58 (28) (2019) 9491–9495.

[14] L. Jiao, Y. Wang, H.-L. Jiang, Q. Xu, Metal-Organic Frameworks as Platforms for Catalytic Applications, Adv. Mater. 30 (2018) 1703663.

[15] J. Li, H. Huang, W. Xue, K. Sun, X. Song, C. Wu, L. Nie, Y. Li, C. Liu, Y. Pan, H.-L. Jiang, D. Mei, C. Zhong, Self-adaptive dual-metal-site pairs in metal-organic frameworks for selective CO_2 photoreduction to CH_4, Nat. Catal. 4 (8) (2021) 719–729.

[16] N. Li, J. Liu, B.-X. Dong, Y.-Q. Lan, Polyoxometalate-Based Compounds for Photo- and Electrocatalytic Applications, Angew. Chem. Int. Ed. 59 (47) (2020) 20779–20793.

[17] M.R. Horn, A. Singh, S. Alomari, S. Goberna-Ferrón, R. Benages-Vilau, N. Chodankar, N. Motta, K. Ostrikov, J. MacLeod, P. Sonar, P. Gomez-Romero, D. Dubal, Polyoxometalates (POMs): from electroactive clusters to energy materials, Energy Environ. Sci. 14 (2021) 1652–1700.

[18] N. Li, J. Liu, J.-J. Liu, L.-Z. Dong, S.-L. Li, B.-X. Dong, Y.-H. Kan, Y.-Q. Lan, Self-Assembly of a Phosphate-Centered Polyoxo-Titanium Cluster: Discovery of the Heteroatom Keggin Family, Angew. Chem. Int. Ed. 58 (48) (2019) 17260–17264.

[19] G.-P. Yang, X.-L. Zhang, Y.-F. Liu, D.-D. Zhang, K. Li, C.-W. Hu, Self-assembly of Keggin-type U(VI)-containing tungstophosphates with a sandwich structure: an efficient catalyst for the synthesis of sulfonyl pyrazoles, Inorg. Chem. Front. 8 (2021) 4650–4656.

[20] G. Yang, K. Li, X. Lin, Y. Li, C. Cui, S. Li, Y. Cheng, Y. Liu, Regio- and Stereoselective Synthesis of (Z)-3-Ylidenephthalides via $H_3PMo_{12}O_{40}$-Catalyzed Cyclization of 2-Acylbenzoic Acids with Benzylic Alcohols, Chin. J. Chem. 39 (2021) 3017–3022.

[21] X.-X. Li, D. Zhao, S.-T. Zheng, Recent advances in POM-organic frameworks and POM-organic polyhedra, Coord. Chem. Rev. 397 (2019) 220–240.

[22] H.L. Nguyen, Reticular Materials for Artificial Photoreduction of CO_2, Adv. Energy Mater. 10 (46) (2020) 2002091.

[23] X.-X. Li, L. Zhang, J. Liu, L. Yuan, T. Wang, J.-Y. Wang, L.-Z. Dong, K. Huang, Y.-Q. Lan, Design of Crystalline Reduction-Oxidation Cluster-Based Catalysts for Artificial Photosynthesis, JACS Au 1 (8) (2021) 1288–1295.

[24] T. Wang, J. Gong, Sacrificing nothing to reduce CO_2, Nat. Energy 5 (9) (2020) 642–643.

[25] B. Qiu, M. Du, Y. Ma, Q. Zhu, M. Xing, J. Zhang, Integration of redox cocatalysts for artificial photosynthesis, Energy Environ. Sci. 14 (10) (2021) 5260–5288.

[26] L. Zhang, X.-X. Li, Z.-L. Lang, Y. Liu, J. Liu, L. Yuan, W.-Y. Lu, Y.-S. Xia, L.-Z. Dong, D.-Q. Yuan, Y.-Q. Lan, Enhanced Cuprophilic Interactions in Crystalline Catalysts Facilitate the Highly Selective Electroreduction of CO_2 to CH_4, J. Am. Chem. Soc. 143 (10) (2021) 3808–3816.

[27] Y. Gao, L. Zhang, Y. Gu, W. Zhang, Y. Pan, W. Fang, J. Ma, Y.-Q. Lan, J. Bai, Formation of a mixed-valence Cu(i)/Cu(ii) metal–organic framework with the full light spectrum and high selectivity of CO_2 photoreduction into CH_4, Chem. Sci. 11 (2020) 10143–10148.

[28] X. Yuan, S. Chen, D. Cheng, L. Li, W. Zhu, D. Zhong, Z.-J. Zhao, J. Li, T. Wang, J. Gong, Controllable Cu^0-Cu^+ Sites for Electrocatalytic Reduction of Carbon Dioxide, Angew. Chem. Int. Ed. 60 (28) (2021) 15344–15347.

[29] W. Wang, C. Deng, S. Xie, Y. Li, W. Zhang, H. Sheng, C. Chen, J. Zhao, Photocatalytic C-C Coupling from Carbon Dioxide Reduction on Copper Oxide with Mixed-Valence Copper(I)/Copper(II), J. Am. Chem. Soc. 143 (7) (2021) 2984–2993.

[30] L. Yuan, S.-F. Hung, Z.-R. Tang, H.M. Chen, Y. Xiong, Y.-J. Xu, Dynamic Evolution of Atomically Dispersed Cu Species for CO_2 Photoreduction to Solar Fuels, ACS Catal. 9 (6) (2019) 4824–4833.

[31] Z.-W. Wang, Y.-Z. Shi, C. Liu, Y.-Y. Kang, L. Wu, Cu^+–Ti^{3+} interface interaction mediated CO_2 coordination model for controlling the selectivity of photocatalytic reduction CO_2, Appl. Catal. B 301 (2022), 120803.

[32] I.A. Weinstock, R.E. Schreiber, R. Neumann, Dioxygen in Polyoxometalate Mediated Reactions, Chem. Rev. 118 (5) (2018) 2680–2717.

[33] Y. Li, E. Wang, S. Wang, Y. Duan, C. Hu, N. Hu, H. Jia, A highly reduced polyoxoanion with phosphorus-centered alternate layers of Mo/V oxides, $[PMo_2{}^{V}Mo_6{}^{VI}V_4{}^{IV}O_{40}(V^{IV}O)_2]^{9-}$, J. Mol. Struct. 611 (1-3) (2002) 185–191.

[34] J.-X. Meng, Y.-G. Li, H. Fu, X.-L. Wang, E.-B. Wang, Controllable self-assembly of two novel metal–organic frameworks based on different tetradentate in situ ligands, CrystEngComm 13 (2) (2011) 649–655.

[35] Y. Yu, H. Ma, H. Pang, S. Li, T. Yu, H. Liu, C. Zhao, Z. Zhang, Two novel zipper-like compounds of the usual and bivanadyl capped Keggin clusters connected by propeller-shaped complexes, New J. Chem. 38 (2014) 1271–1276.

[36] J. Liu, Y. Liu, N. Liu, Y. Han, X. Zhang, H. Huang, Y. Lifshitz, S.-T. Lee, J. Zhong, Z. Kang, Metal-free efficient photocatalyst for stable visible water splitting via a two-electron pathway, Science 347 (2015) 970–974.

[37] J. Hong, W. Zhang, J. Ren, R. Xu, Photocatalytic reduction of CO_2: a brief review on product analysis and systematic methods, Anal. Methods 5 (2013) 1086–1097.

[38] Y.-X. Pan, Y.a. You, S. Xin, Y. Li, G. Fu, Z. Cui, Y.-L. Men, F.-F. Cao, S.-H. Yu, J. B. Goodenough, Photocatalytic CO_2 Reduction by Carbon-Coated Indium-Oxide Nanobelts, J. Am. Chem. Soc. 139 (11) (2017) 4123–4129.

[39] H. Lin, Z. Ma, J. Zhao, Y. Liu, J. Chen, J. Wang, K. Wu, H. Jia, X. Zhang, X. Cao, X. Wang, X. Fu, J. Long, Electric-Field-Mediated Electron Tunneling of Supramolecular Naphthalimide Nanostructures for Biomimetic H_2 Production, Angew. Chem. Int. Ed. 60 (3) (2021) 1235–1243.

[40] Z.-B. Fang, T.-T. Liu, J. Liu, S. Jin, X.-P. Wu, X.-Q. Gong, K. Wang, Q.i. Yin, T.-F. Liu, R. Cao, H.-C. Zhou, Boosting Interfacial Charge-Transfer Kinetics for Efficient Overall CO_2 Photoreduction via Rational Design of Coordination Spheres on Metal-Organic Frameworks, J. Am. Chem. Soc. 142 (28) (2020) 12515–12523.

[41] H.-N. Wang, Y.-H. Zou, H.-X. Sun, Y. Chen, S.-L. Li, Y.-Q. Lan, Recent progress and perspectives in heterogeneous photocatalytic CO_2 reduction through a solid–gas mode, Coord. Chem. Rev. 438 (2021), 213906.

[42] M. Zhang, J.-N. Chang, Y. Chen, M. Lu, T.-Y. Yu, C. Jiang, S.-L. Li, Y.-P. Cai, Y.-Q. Lan, Controllable Synthesis of COFs-Based Multicomponent Nanocomposites from Core-Shell to Yolk-Shell and Hollow-Sphere Structure for Artificial Photosynthesis, Adv. Mater. 33 (2021) 2105002.

[43] B. Wang, J. Di, L. Lu, S. Yan, G. Liu, Y. Ye, H. Li, W. Zhu, H. Li, J. Xia, Sacrificing ionic liquid-assisted anchoring of carbonized polymer dots on perovskite-like $PbBiO_2Br$ for robust CO_2 photoreduction, Appl. Catal. B 254 (2019) 551–559.

[44] S. Barman, A. Singh, F.A. Rahimi, T. k., Maji Metal-Free Catalysis: A Redox-Active Donor-Acceptor Conjugated Microporous Polymer for Selective Visible-Light-Driven CO_2 Reduction to CH_4, J. Am. Chem. Soc. 143 (2021) 16284–16292.

[45] Y. Cao, L. Guo, M. Dan, D.E. Doronkin, C. Han, Z. Rao, Y. Liu, J. Meng, Z. Huang, K. Zheng, P. Chen, F. Dong, Y. Zhou, Modulating electron density of vacancy site by single Au atom for effective CO_2 photoreduction, Nat Commun 12 (2021) 1675.

[46] Z. Wu, H. Wu, W. Cai, Z. Wen, B. Jia, L. Wang, W. Jin, T. Ma, Engineering Bismuth-Tin Interface in Bimetallic Aerogel with a 3D Porous Structure for Highly Selective Electrocatalytic CO_2 Reduction to HCOOH, Angew. Chem. Int. Ed. 60 (22) (2021) 12554–12559.

[47] X.-F. Qiu, H.-L. Zhu, J.-R. Huang, P.-Q. Liao, X.-M. Chen, Highly Selective CO_2 Electroreduction to C_2H_4 Using a Metal-Organic Framework with Dual Active Sites, J. Am. Chem. Soc. 143 (19) (2021) 7242–7246.

[48] J.-D. Yi, R. Xie, Z.-L. Xie, G.-L. Chai, T.-F. Liu, R.-P. Chen, Y.-B. Huang, R. Cao, Highly Selective CO_2 Electroreduction to CH_4 by In Situ Generated Cu_2O Single-Type Sites on a Conductive MOF: Stabilizing Key Intermediates with Hydrogen Bonding, Angew. Chem. Int. Ed. 59 (2020) 23641–23648.

[49] X. Li, Y. Sun, J. Xu, Y. Shao, J.u. Wu, X. Xu, Y. Pan, H. Ju, J. Zhu, Y.i. Xie, Selective visible-light-driven photocatalytic CO_2 reduction to CH_4 mediated by atomically thin $CuIn_5S_8$ layers, Nat. Energy 4 (8) (2019) 690–699.

[50] Y. Xi, X. Zhang, Y. Shen, W. Dong, Z. Fan, K. Wang, S. Zhong, S. Bai, Aspect ratio dependent photocatalytic enhancement of $CsPbBr_3$ in CO_2 reduction with two-dimensional metal organic framework as a cocatalyst, Appl. Catal. B 297 (2021), 120411.

[51] D.-L. Meng, M.-D. Zhang, D.-H. Si, M.-J. Mao, Y. Hou, Y.-B. Huang, R. Cao, Highly Selective Tandem Electroreduction of CO_2 to Ethylene over Atomically Isolated Nickel-Nitrogen Site/Copper Nanoparticle Catalysts, Angew. Chem. Int. Ed. 60 (48) (2021) 25485–25492.